15 Phase transitions and superconducting photon detectors

X. Zhang, F. von Rohr, H. Grundmann, O. Bossen, S. Siegrist, A. Engel and A. Schilling

in collaboration with: University of Bern (K. Krämer), Karlsruhe Institut für Technologie (K. Il'in), Deutsches Zentrum für Luft- und Raumfahrt (H.-W. Hübers, A. Semenov), FIRST Lab ETH Zürich, PSI Villigen (M. Medarde, K. Conder), McMaster University (H. Dabkowska), IFW Dredsen (V. Kataev, A. Alfonsov), University of S ao Paulo (A. Paduan-Filho), Institute of Nuclear Physics, Tashkent (A. Rakhimov), ETH Zürich (R. Nesper & J. Novotny), Princeton University (R. J. Cava)

(PTMA)

15.1 Superconducting nanowire single-photon detectors for optical and X-ray photons

In recent years there has been growing evidence that magnetic vortices are important for a proper understanding of the working principle of superconducting nanowire single-photon detectors (SNSPD) (see, for example, last year's annual report, in which we reported the first systematic measurements of the magnetic-field dependence of dark counts of SNSPD [1]). Our measurements strongly supported the idea that vortices entering and crossing the superconducting strip are the main contribution to dark counts in SNSPD [2]. A later study [3] showed that there is a magnetic-field dependence on the photon counts as well, which, however, is not described by the currently accepted model. Since there is no comprehensive description of the detection mechanism in SNSPD, we developed a simple, numerical model [5] that is detailed enough to capture the physics in SNSPD and to describe experimental results [4]. Two coupled differential equations describing the generation and the diffusion of quasi-particles after the absorption of a photon are solved numerically. The resulting quasi-particle distributions (shown in Fig. 15.1(a)) are used to compute the current distribution as a function of time, shown in Fig. 15.1(b) for t=2.6 ps. These results can be compared with the outcome of two alternative, analytic detection models ("hard-core model" [6] and "quasi-particle model" [7]). They strongly support a detection mechanism by photon-assisted vortex-crossings which requires lower photon energies than the other detection models for a given experimental situation. In the case of sufficiently high photon energies, such vortex crossings always trigger the formation of the initial normal-conducting cross-section, well before the competing mechanisms would lead to a photon detection event. Furthermore, only the results of the

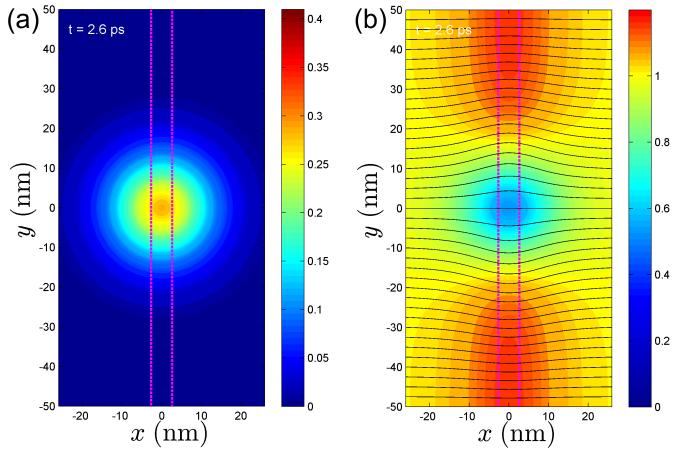

FIG. 15.1 – Results from our calculations for the spatial distributions of the quasi-particles (a) and the current density (b), 2.6 ps after the absorption of a photon with wavelength $\lambda = 1$ μm in a superconducting strip. The process results in an increase of the current density near the edges of the superconducting strip. The dashed vertical lines outline a ξ-slab, the minimum volume that must become normal-conducting in order to trigger a detection event.

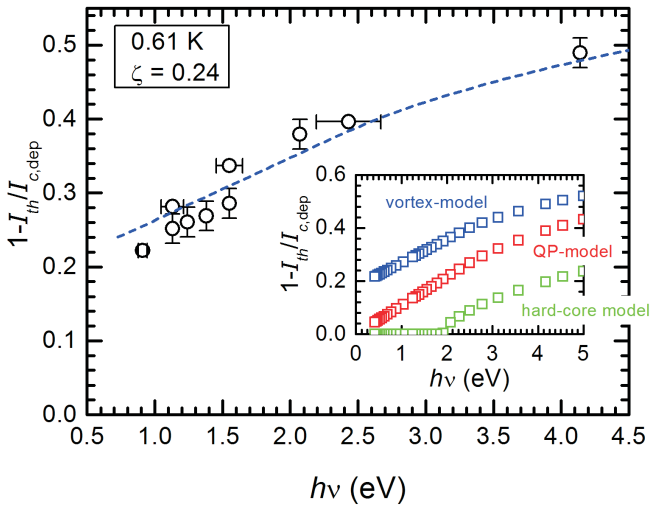

FIG. 15.2 – $1 - I_{th}/I_{c,dep}$ vs. photon energy, where I_{th} is the minimum or threshold bias current and $I_{c,dep}$ the critical depairing-current. Measured values are compared with our simulation results (dashed blue). The quasi-particle multiplication efficiency ζ was the only free parameter in the fit. The inset compares our model with two other models.

vortex-crossing model are consistent with our experimentally determined detector characteristics, *i.e.*, the dependence of the minimum bias current on photon energy (see Fig. 15.2). A very recent detailed study of this kind of detection criterion [8] has confirmed the observed agreement with experiments over a very large range of photon energies.

[1] A. Engel, A. Schilling, K. Il'in, and M. Siegel, Phys. Rev. B, **86**, (2012) 140506(R).

[2] L.N. Bulaevskii *et al.*, Phys. Rev. B, **83**, (2011) 144526.

[3] R. Lusche *et al.*, Phys. Rev. B, **89**, (2014) 104513.

[4] L.N. Bulaevskii, M.J. Graf, and V.G. Kogan, Phys. Rev. B, **85**, (2012) 014505.

[5] A. Engel and A. Schilling, J. Appl. Phys., **114**, (2013) 214501.

[6] G.N. Gol'tsman *et al.*, Appl. Phys. Lett., **79**, (2001) 705.

[7] A. Semenov, A. Engel, H.W. Hübers, K. Il'in, and M. Siegel, Eur. Phys. J. B, **47**, (2005) 495.

[8] J.J. Renema *et al.*, Phys. Rev. Lett., **112**, (2014) 117604.

15.2 Ac-magnetic susceptibility in the peak-effect region of Nb_3Sn

We performed a systematic study of the ac-magnetic susceptibility on an Nb_3Sn single crystal, which displays a strong peak effect near the upper critical field H_{c2} (in collaboration with N. Toyota, Tohoku University, Japan). In external magnetic fields above $\mu_0 H \approx 3$ T, the peak effect manifests itself in a single, distinct peak in the real part $\chi'(T)$ of the ac susceptibility as a function of temperature T, the size of which continuously increases with increasing magnetic field H. In the imaginary part $\chi''(T)$ of the ac susceptibility, on the other hand, a single peak initially grows with increasing H up to a well-defined value, and then splits into two sharp peaks which separate when H is further increased (see Fig. 15.3).

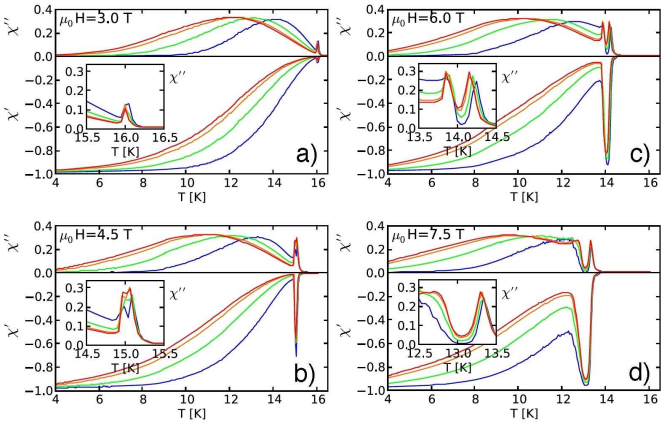

FIG. 15.3 – ac-Magnetic susceptibility data of an Nb_3Sn single crystal. The magnetic field $\mu_0 H \approx 3$ T (panel (a)) corresponds to case b) in Fig. 15.4, and the data taken at larger fields (panels (b) to (d)) to case c).

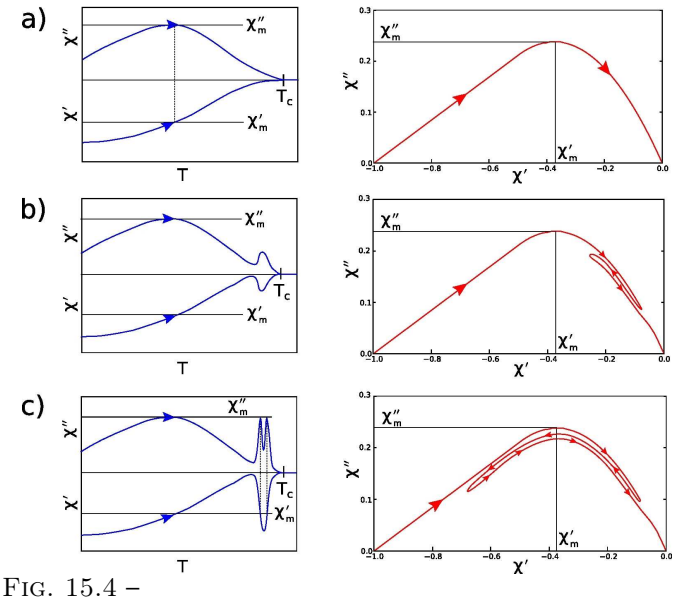

FIG. 15.4 – Left panels: Real and imaginary parts of the ac-magnetic susceptibility for a superconductor displaying a peak effect. Right panels: corresponding χ'' *vs.* χ' representations. Arrows indicate an experiment with increasing temperature.
a): a type II superconductor without peak effect;
b): a type II superconductor with a weak peak effect, producing single peaks in both real and imaginary parts of the ac susceptibility;
c): a type II superconductor showing a strong peak effect, leading to a single peak in the real part but a double-peak structure in the imaginary part.

We could explain this surprising behavior by a flux-creep model and taking into account the enhancement of the critical-current density in the peak-effect region near T_c in which Bean's critical-state model seems to apply [1].

To illustrate the occurrence of single- and double peak structures in $\chi''(T)$ we are plotting a $\chi''(\chi')$ relationship in the right panels of Fig. 15.4, as it is typically assumed in superconductors near T_c. In most known cases, $\chi''(\chi')$ is a single-valued function with a maximum χ''_m for a certain value of χ'_m. Without any peak effect, the critical-current density $j_c(T)$ decreases monotonically with increasing temperature T (direction indicated in Fig. 15.4) and vanishes at $T \sim T_c$. As a result, the real part χ' of the magnetic susceptibility also monotonically increases with T before reaching zero at T_c (see Fig. 15.4a, left panel). If the sample displays a peak effect near T_c, however, the critical-current density increases sharply before dropping to zero at the transition to the normal state [2–4]. This causes a sudden decrease in $\chi'(T)$ near T_c, *i.e.*, a peak in $|\chi'(T)|$ (Figs. 15.4b and c, left panels). Depending on

the magnitude of this peak which is determined by the pinning strength in the peak-effect region, the sample geometry and the probing ac magnetic field, this will either lead to a single peak in the imaginary part $\chi''(T)$ of the susceptibility if $|\chi'| \leq |\chi'_m|$ (Fig. 15.4b), or to a double-peak structure as soon as $|\chi'| > |\chi'_m|$ in the peak effect region (Fig. 15.4c).

A refined analysis of our data also revealed that the crystal is in the so-called "flux-creep regime" below the peak-effect region (*i.e.*, in a region in which a non-equilibrium magnetic-flux distribution relaxes to equilibrium on testable laboratory time scales), while in the peak-effect region, the "Bean critical state" is realized, *i.e.*, a state in which a non-equilibrium magnetic-flux distribution can be quasi-stationary [1].

[1] O. Bossen, A. Schilling and N. Toyota, Physica C, **492** (2013) 133.

[2] T.G. Berlincourt, R.R. Hake and D.H. Leslie, Phys. Rev. Lett., **6**, (1961) 671.

[3] M.A.R. LeBlanc and W.A. Little in *Proceedings of the 7th International Conference on Low Temperature Physics*, p. 364, University of Toronto Press, (1961).

[4] A. B. Pippard, Philos. Mag., **19** (1969) 217.

15.3 Influence of disorder on the structural phase transition and magnetic interactions in $Ba_{3-x}Sr_xCr_2O_8$

in collaboration with: Paul Scherrer-Institut Villigen (PSI): Marisa Medarde-Barragan, Denis Sheptyakov

In the previous annual report, we reported on the peculiar change of the magnetic interactions in the spin dimer system $Ba_{3-x}Sr_xCr_2O_8$ as a function of the Sr content x. An analysis of the temperature dependence of the magnetization $M(T)$ suggested that the intra-dimer interaction constant J_0 changes in a non-linear way with x[1].

To probe possible structural explanations for the reported change of J_0, we have performed neutron powder diffraction experiments at room temperature and at $T = 2$ K for various values of x at the *High-Resolution Powder Diffractometer for Thermal Neutrons*, HRPT (PSI, Villigen). For $x \in \left\{0, \frac{1}{3}, \frac{7}{3}, 3\right\}$, our analysis suggests a breaking of the threefold rotational symmetry around the dimer axis with decreasing temperature. The corresponding change of the space group from $R\bar{3}m$ at room temperature to $C_{2/c}$ at $T = 2$ K is indicated by the appearance of additional diffraction peaks (see Fig. 15.5). This symmetry breaking, which lifts the orbital degeneracy of the

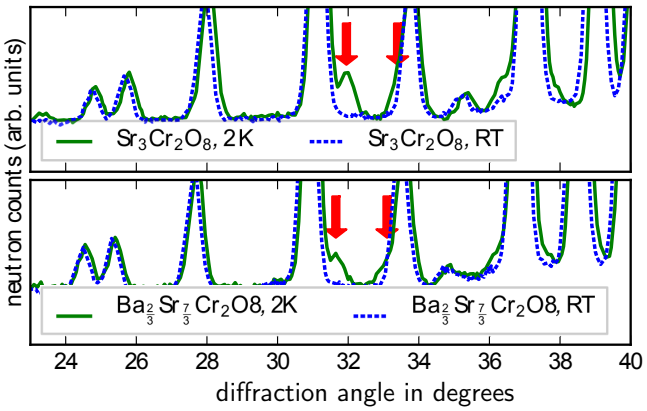

FIG. 15.5 – Additional peaks appearing in the low temperature neutron diffractograms for $Sr_3Cr_2O_8$ and $Ba_{\frac{2}{3}}Sr_{\frac{7}{3}}Cr_2O_8$, indicating the structural phase transition.

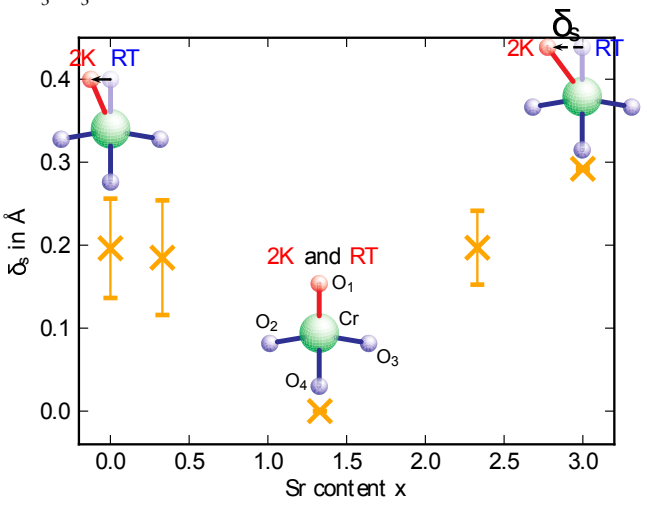

FIG. 15.6 – Distance δ_s of the apical oxygen atom from the dimer axis as a function of the Sr content x. The distance in the corresponding sketch is exaggerated for visual clarity.

Cr^{5+}-ion that is surrounded by an oxygen tetrahedron, has previously been reported for the mother compounds $Ba_3Cr_2O_8$[2] and $Sr_3Cr_2O_8$[3]. It is essentially based on a Jahn-Teller like shift of the apical atom of this tetrahedron away from the symmetry axis (see Fig. 15.6). We found that the value δ_s of this shift depends on the Sr content x and vanishes for $x = \frac{4}{3}$.

The strength of J_0 is mainly given by the exchange energy between the Cr^{5+}-ions. A shift of the oxygen position changes this energy and should therefore strongly influence J_0. Based on the obtained detailed information on the crystallographic structure, we have therefore performed extended Hückel tight binding (ETHB) calculations in order to examine the theoretical value for J_0 at room temperature and $T = 2$ K. As shown in Fig. 15.7, the experimental values for J_0 can be well reproduced by our calculations based on the low temperature structure for all values of x, as reported for pure $Sr_3Cr_2O_8$ [3]. In contrast to that, the room temperature calculations differ substantially from the experimental values for

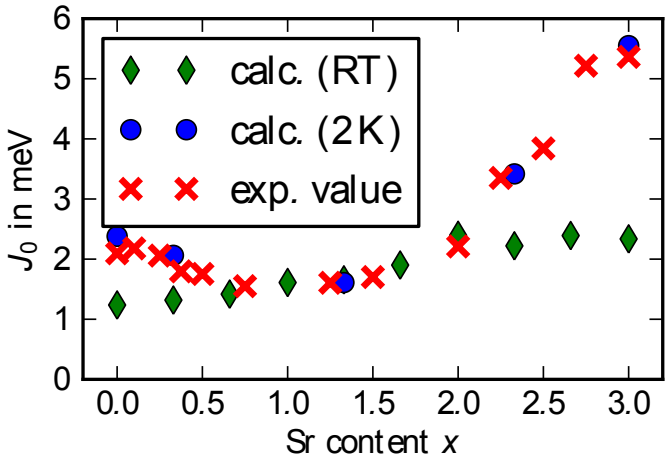

FIG. 15.7 – Intra-dimer interaction constant J_0 for $Ba_{3-x}Sr_xCr_2O_8$ as a function of the Sr content x. The data are obtained from SQUID-measurements (exp.) and estimated based on EHTB-calculations for the crystal structure at room temperature and $T = 2$ K (calc.).

those values of x for which a symmetry breaking could be observed. Hence, we conclude that a gradual disappearance of the Jahn-Teller induced symmetry breaking is responsible for the peculiar minimum of J_0 for intermediate values of x.

Our analysis of the crystal structure shows that all crystallographic parameters vary smoothly and in a strictly monotonous way as functions of x, providing no direct reason for a suppressed Jahn-Teller distortion for intermediate values of x. However, due to the gradual substitution of Ba by Sr, chemical disorder is introduced into the system. The Ba- and Sr-atoms are randomly distributed over the possible atomic positions, changing the local stoichiometry between different unit cells. This random distribution leaves the symmetry group intact *on global average*, but breaks it locally. This local symmetry breaking gradually lifts the orbital degeneracy of the Cr^{5+}-ions so that the possible energy gain through a breaking of the symmetry is reduced, thereby suppressing the Jahn-Teller transition. See [4] for further details.

[1] H. Grundmann *et al.*, Mat. Res. Bul., **48** (2013) 3108.

[2] M. Kofu *et al.*, Phys. Rev. Lett., **102** (2009) 037206.

[3] L. C. Chapon *et al.*, arXiv:0807.0877v2.

[4] H. Grundmann, M. Medarde, D. Sheptyakov and A. Schilling, submitted to Phys. Rev. B.

15.4 Superconductivity and charge-density-wave ordering in $BaTi_2Sb_2O$

Recent studies have shown that $BaTi_2Sb_2O$ exhibits a transition to a density wave ordered state at $T_{DW} \approx 55$ K, and a transition to a bulk superconducting state at $T_c \approx 1$ K [1, 2]. $BaTi_2Sb_2O$ belongs to a large family of stacked, layered titanium oxide pnictide compounds. In these compounds the nominal valence of titanium is Ti^{3+} with its 3d orbitals singly occupied. In this $3d^1$ configuration, Ti is surrounded octahedrally by O and Sb, forming a Ti_2O square sub-lattice. From a structural and chemical perspective, these Ti_2O layers can be interpreted as the $3d^1$-anti-configuration of the $3d^9$ CuO_2 planes in the cuprates.

For the systematic investigation of the physical properties of this material, we have successfully prepared $BaTi_2Sb_2O$ and $Ba_{1-x}A_xTi_2Sb_2O$ (A = Na, Rb) solid solutions by high-temperature solid-state reactions up to 1000 °C. [3, 4] We have used the substitution of Ba by an alkaline earth metal as a strategy to hole-dope and therefore manipulate the Fermi-level of these compounds. In Fig. 15.8 we show the x-ray diffraction pattern at ambient temperature for the sample of nominal composition $Ba_{0.7}Rb_{0.3}Ti_2Sb_2O$ ($x = 0.3$), together with the crystal structure of the compound in the inset. All compounds of the $Ba_{1-x}A_xTi_2Sb_2O$ solid solutions were found to belong to the same crystal

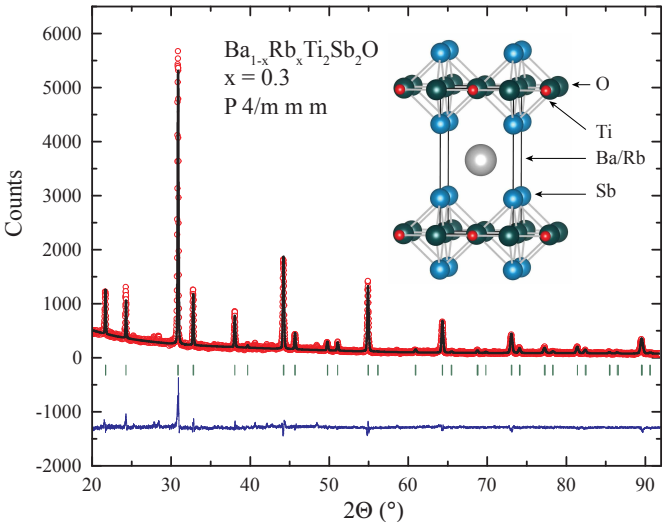

FIG. 15.8 – The powder x-ray diffraction pattern at ambient temperature for the sample of nominal composition $Ba_{0.7}Rb_{0.3}Ti_2Sb_2O$ ($x = 0.3$). The crystal structure ($CeCr_2Si_2C$-type) of the compound is shown in the inset. The vertical dark green lines show the theoretical Bragg peak positions for this phase. The blue pattern on the bottom is the difference plot between the theoretical pattern and the observed intensities.

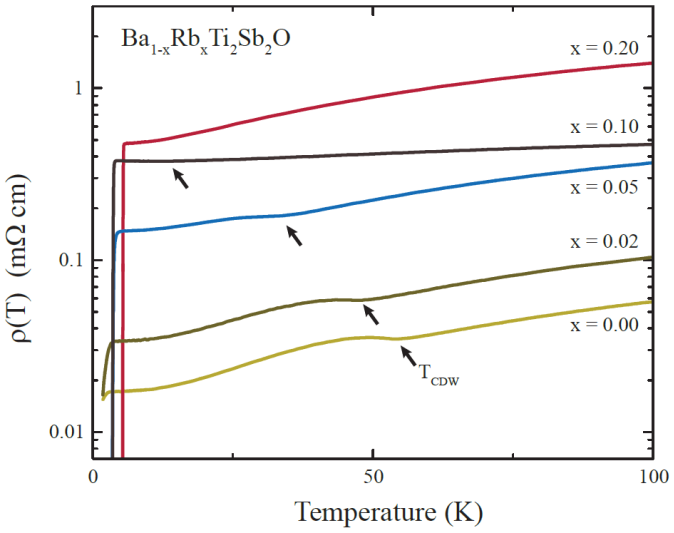

FIG. 15.9 – Resistivities of $Ba_{1-x}Rb_xTi_2Sb_2O$ for $x = 0$, 0.02, 0.05, 0.1, and 0.2 in a temperature range between 1.8 K and 100 K. The CDW transition manifests itself in a sudden increase of the resistivity for the samples $x = 0$, 0.02, 0.05 and 0.1 (marked with a black arrow). This anomaly is absent for the sample with $x = 0.2$. For increasing rubidium contents x (up to $x = 0.2$), the normal state resistivities increase, the CDW ordering transition temperatures T_{CDW} decrease, while the critical temperatures T_c increase.

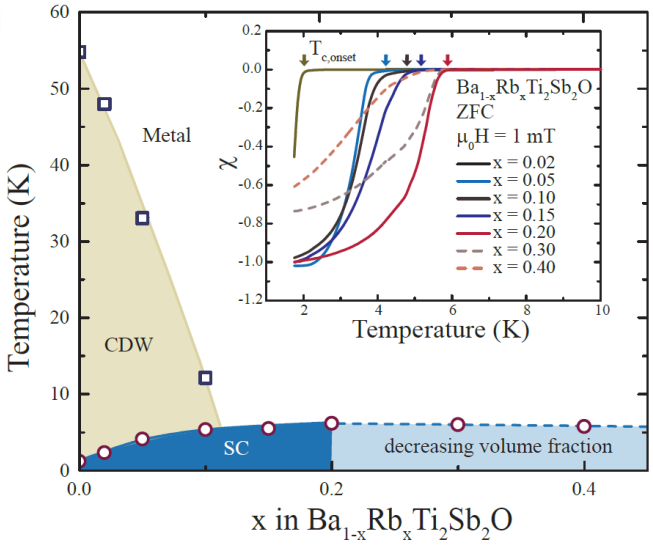

FIG. 15.10 – Phase diagram of the electronic properties of $Ba_{1-x}Rb_xTi_2Sb_2O$ derived from resistivity and magnetization measurements.

structure, which is isopointal to the $CeCr_2Si_2C$-type structure ($P4/mmm$). Within the $Ba_{1-x}Rb_xTi_2Sb_2O$ solid solution $0 \leq x \leq 0.4$ the cell parameter vary only slightly, but continuously with increasing rubidium content.

The resistivities $\rho(T)$ of $Ba_{1-x}Rb_xTi_2Sb_2O$ with $x = 0$, 0.05, 0.1, and 0.2 in a temperature range of $T = 1.8$ K to 100 K are shown in Fig. 15.9. The parent compound ($x = 0$), shows a distinct kink in the resistivity at T_{CDW} = 55 K, which is a characteristic feature of a DW transition. This phase transition temperature T_{DW} is strongly reduced and eventually suppressed with increasing rubidium content. For a relatively small doping of $x = 0.05$ the DW transition is already lowered to 34 K, whereas the critical temperature is increased by more than 2 K to T_c = 3.7 K. Taking the absolute value of the resistivity as a measure for the metallicity of a sample, we can state that the increase of the superconducting transition T_c and the decrease and subsequent suppression of the CDW ordering temperature T_{CDW} go along with a decrease in metallicity.

In Fig. 15.10 we summarize the electronic phase diagram of the $Ba_{1-x}Rb_xTi_2Sb_2O$ solid solution. The critical temperatures T_c used for the phase diagram are the intersections of the slopes of the phase transitions and the normal state magnetizations.

In a series of μSR experiments we have probed the density wave transition and superconducting properties of $BaTi_2Sb_2O$ and the $Ba_{1-x}Na_xTi_2Sb_2O$ (with $x = 0.05$, 0.1, 0.15, 0.2, 0.25, 0.3) solid solution [4]. The zero-filed (ZF) and transverse-field (TF) muon time signals for the parent compound $BaTi_2Sb_2O$ were measured well above $T_{DW} \approx$ 50 K at $T = 100$ K and below at $T = 1.5$ K. The zero field μSR spectra above and below T_{DW} do not exhibit any noticeable change in the relaxation rate, indicating the absence of a spontaneous internal field at the muon stopping site. This is further supported by the weak TF measurements, where no reduction of the asymmetry is observed, as it would be expected in case of magnetic ordering. Therefore, we can exclude that the observed transition at T_{DW} is caused by spin density wave (SDW) ordering in the parent compound $BaTi_2Sb_2O$ as speculated earlier [1, 5]. The observed transition is therefore most likely caused by CDW ordering.

For the optimally doped sample $Ba_{0.8}Na_{0.2}Ti_2Sb_2O$ with a $T_c \approx 5.1$ K, we have performed ZF and TF μSR experiments at $T = 1.5$ K and above T_c at 6 K. The observed strong additional relaxation in the TF measurements below T_c is caused by the formation of the flux-line lattice (FLL) in the Shubnikov phase, as depicted in Fig. 15.11. In Fig. 15.12 we show the temperature dependence of $\lambda^{-2}(T)$ as reconstructed from the Gaussian relaxation rate $\sigma_{sc}(T)$. These measurements suggest that λ^{-2} is virtually temperature independent below $T \simeq 1$ K for the optimally doped sample. The obtained experimental temperature dependence of $\lambda^{-2}(T)$ agrees well with the clean limit approach for a London superconductor with an s-wave gap.

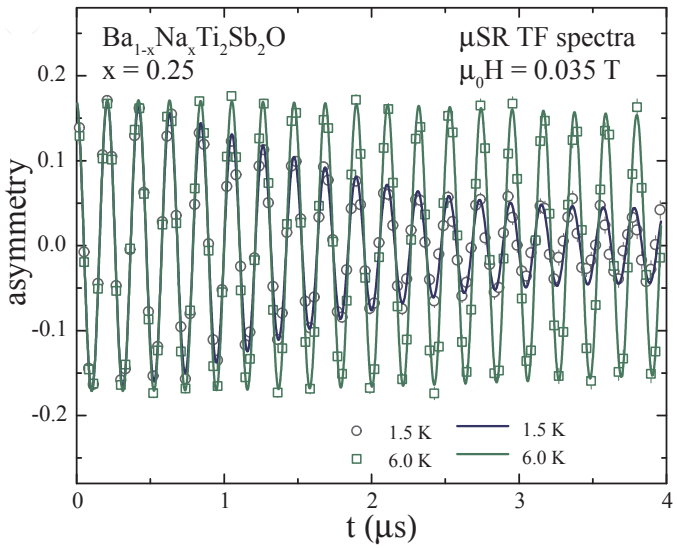

FIG. 15.11 – The TF μSR spectra for $x = 0.25$ above (6 K) and below (1.5 K) T_c. The strong relaxation of the signal at 1.5 K can be ascribed to the presence of the flux-line lattice.

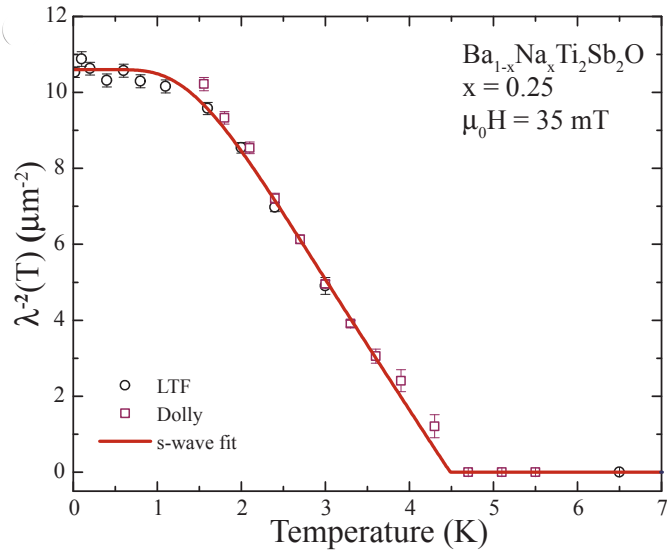

FIG. 15.12 – The temperature dependence of λ^{-2} for $x = 0.2$ as reconstructed from $\sigma_{sc}(T)$, measured in $\mu_0 H = 35$ mT. The solid line corresponds to an conventional London superconductor with an s-wave gap with $2\Delta/(k_B T_c) = 2.9$. Squares: Dolly instrument, circles: LTF instrument.

In our studies we have shown how superconductivity and DW ordering evolve in $Ba_{1-x}Rb_xTi_2Sb_2O$ as a function of the substitution of barium by rubidium. We have evidenced that the density wave ordering transition T_{DW} is continuously lowered and eventually suppressed with increasing rubidium content, while the transition temperature to superconductivity, T_c, is increased, reaching a maximum $T_{c,max}$ = 5.4 K. Our results support the scenario that hole doping by the incorporation of Na^+, K^+, and also Rb^+ is of great importance for the suppression of CDW ordering and the occurrence of superconductivity in these materials. [5, 6] From our μSR studies we are able to conclude that the phase transition observed in the normal state of these compounds is of CDW character, and from our low temperature μSR data we have found evidence for ruling out some scenarios about the microscopic origin of superconductivity in these compounds. The obtained experimental temperature dependence of $\lambda^{-2}(T)$ can be reasonably well explained within the clean limit approach for a conventional London superconductor. We find $BaTi_2Sb_2O$ to be a versatile model-system for the investigation of the competition and coexistence of conventional superconductivity and CDW ordering.

[1] T. Yajima *et al.*, JPSJ, **82** (2013) 103706.

[2] M. Gooch *et al.*, Phys. Rev. B, **88** (2013) 064510.

[3] F. von Rohr, R. Nesper and A. Schilling, Phys. Rev. B, **89** (2014) 094505.

[4] F. von Rohr *et al.*, Phys. Rev. B, **88** (2013) 140501(R).

[5] P. Doan *et al.*, JACS, **134** (2012) 16520.

[6] U. Pachmayr and D. Johrendt, Solid State Sciences, **28** (2014) 31.